minerals

MDPI

Article

Mineralogical and Crystal-Chemical Constraints on the Glauconite-Forming Process in Neogene Sediments of the Lower Guadalquivir Basin (SW Spain)

Sandra Fernández-Landero and Juan Carlos Fernández-Caliani *

Department of Earth Sciences, University of Huelva, 21071 Huelva, Spain; sandra.fernandez@dct.uhu.es
* Correspondence: caliani@uhu.es

Abstract: Glaucony is a significant green marine facies in the northwestern passive margin of the Guadalquivir Basin (Spain), where glauconite formed authigenically on a sediment-starved continental shelf, with fecal pellets and benthic foraminiferal tests being the main glauconitized substrates. Results from a study using XRD, TGA-DSC, SEM-EDS, and EPMA have revealed that glauconite is remarkably heterogeneous in mineral composition and chemical maturity, even in a single grain, reflecting a complex interaction of micro-environmental factors, substrate influences and post-depositional alterations. In its early stage, the glauconitization process is consistent with the slow precipitation of a Fe-rich smectite phase, most likely intergrade between nontronite and Fe-montmorillonite end-members, which evolved to a regularly interstratified glauconite-smectite (Gl/S). The Fe-smectite-to-Gl/S transformation is interpreted as a diffusion-controlled reaction, involving sufficient Fe availability in pore water and the constant diffusive transport of seawater K^+ and Mg^{2+} ions towards the substrate. The pelletal glauconite is actually a highly evolved Gl/S consisting almost totally of mica layers, with 0.74 ± 0.05 apfu of K^+ in the interlayer, while the Gl/S occurring as replacements of foraminiferal tests contains a mean of 7% of expandable layers in the walls and 16% in the chamber fillings, due to rate-limited ion diffusion.

Keywords: glaucony; green marine clays; authigenesis; glauconitization; glauconite-smectite mixed layer

Citation: Fernández-Landero, S.; Fernández-Caliani, J.C. Mineralogical and Crystal-Chemical Constraints on the Glauconite-Forming Process in Neogene Sediments of the Lower Guadalquivir Basin (SW Spain). *Minerals* **2021**, *11*, 578. https://doi.org/10.3390/min11060578

Academic Editors: Ana I. Ruiz and Jaime Cuevas Rodríguez

Received: 7 May 2021
Accepted: 26 May 2021
Published: 28 May 2021

1. Introduction

Glauconite is a series name of Fe-rich interlayer-deficient dioctahedral micas with a representative formula of $K_{0.8}R^{3+}{}_{1.33}R^{2+}{}_{0.67}Al_{0.13}Si_{3.87}O_{10}(OH)_2$ [1], in which the ratio $^{VI}R^{2+}/(^{VI}R^{2+} + {}^{VI}R^{3+})$ is greater than or equal to 0.15, the ratio $^{VI}Al/(^{VI}Al + {}^{VI}Fe^{3+})$ is lesser than or equal to 0.5, and the total interlayer cations (mostly K^+) comprise between 0.60 and 0.85 atoms per formula unit (apfu). Recently, glauconite has been described as a mica-rich mica-smectite (R3 ordered) mixed layer mineral, with pure end-member glauconitic mica having up to 0.8 apfu of K^+ in the interlayer space [2].

The term glaucony was introduced by Odin and Létolle [3] to designate a green marine facies, composed mainly of sand-sized glauconitic grains, commonly reported in transgressive deposits and condensed sections, in association with phosphate grains and abundant fossils. Hence, glauconite authigenesis is regarded as a powerful indicator tool for basin analysis and stratigraphic correlation purposes [4], as well as a reliable paleoenvironmental indicator for climate history [5]. It is generally agreed that glauconitization is an authigenic process that typically develops in marine settings, on the outer margins of continental shelves and adjacent slope areas with low sedimentation rates [6], although ancient glaucony has also been reported in shallow-marine depositional environments, including estuaries and coastlines [7].

Over the past decades, the glauconitization process has been revisited by many authors, and a variety of models have been postulated to explain the origin and compositional evolution of glauconite, including: (1) the "layer lattice" theory [8,9], which assumes a

conversion of degraded 2:1 clay mineral to a newly formed Fe- and K-rich glauconitic mineral, under reducing conditions, with the simultaneous increase of K and Fe contents; (2) the "verdissement" theory [6,10], which involves the initial precipitation of K-poor and Fe-rich smectite within porous substrates, usually biogenic clasts or fecal pellets, and the subsequent dissolution and recrystallization of the substrate with increasing fixation of K at constant Fe content, evolving through four successive maturation stages; and (3) the "pseudomorphic replacement" theory, which implies dissolution and replacement of a pre-existent K-rich mineral grain (e.g., K-feldspar) with highly variable Fe content, regardless of whether the original substrate is porous or non-porous, as proposed by Dasgupta et al. [11]. So far, the precipitation-dissolution-recrystallization theory is the most widely accepted explanation for the origin and evolution of glauconite.

Although glauconite has been studied extensively, it continues to attract a high level of research interest. Substantial progress has been achieved in understanding the depositional environment, sedimentary conditions, and paleogeographical implications of glaucony (for a review see [7]), but there is still debate about the true mineralogical nature of glauconite, and the precise process and microenvironment of formation still remain poorly understood [12]. Moreover, the origin of the grain-scale compositional heterogeneity has usually been overlooked or has not been addressed in sufficient detail.

In this paper, we report a comprehensive study focusing on the process of glauconitization of fecal pellets and foraminiferal tests in a passive-margin condensed section of the lower Guadalquivir Basin (SW Spain), by integrating XRD, TGA-DSC, SEM-EDS, and EPMA data. The aims of the research were to: (1) identify the factors controlling the source, (geo)availability and geochemical behavior of iron and other major elements needed for glauconite formation; (2) constrain the overall glauconite-forming process in terms of mineral chemistry; (3) determine the influence of the host substrate on the chemical variability and maturity of glauconite; and (4) assess the post-depositional weathering effects on glauconite composition.

2. Geological Setting

The area selected for a detailed study of glauconite is geologically located in the westernmost sector of the Guadalquivir Basin, a Neogene foreland basin situated between the Paleozoic rocks of the Variscan Iberian Massif northward and the external units of the Betic Ranges to the south (Figure 1a). The sedimentary infill of the Guadalquivir Basin comprises five off-lapping depositional sequences, namely, A, B, C, D and E, that are progressively younger to the west, ranging in age from the Upper Miocene to the Quaternary [13].

At the western edge of the Guadalquivir Basin, the Neogene deposits have been divided into four sedimentary formations from bottom to top, as follows [14–16]: (1) the Niebla Formation (Upper Tortonian), made up of mixed carbonate-siliciclastic deposits; (2) the Gibraleón Clay Formation (Upper Tortonian–Lower Pliocene), formed by a monotonous succession of greenish-bluish clays and marls; (3) the Huelva Sands Formation (Lower Pliocene), characterized by densely fossiliferous sandy deposits; and (4) the Bonares Sands Formation (attributed to the Upper Pliocene–Lower Pleistocene), composed of coarse-grained sands that grade upwards into pebble conglomerates. These Neogene formations correspond, in whole or in part, to the regional depositional sequences B, C, D and E, respectively.

Two distinctive glauconite-rich levels occur at the base of both the Gibraleón Clay and the Huelva Sands Formations, within stratigraphically condensed intervals formed during major transgressive events, which have been interpreted to reflect periods of very low rates of sedimentation [17,18]. The lower glauconitic horizon has been radiometrically dated at 6.7 $\pm$ 0.3 Ma [19], close to the Tortonian–Messinian transition, while the upper one is assigned to the Lower Pliocene, based on fossil evidence [14]. It must be noted that glauconite continues to be formed in the present day on the outer shelf adjacent to the study area [20].

The stratigraphic section of the Neogene deposits exposed in the area (Figure 1b,c) consists of a coarsening upward sequence of clays, white sandy silts and glauconitic sands (Upper Miocene), which are erosively overlain by siliciclastic deposits of Early Pliocene age [21]. The contact between the glauconite-bearing horizon (up to 3 m thick) and the underlying sediments appears intensely bioturbated, with biogenic structures (burrows) filled with glauconite. The Neogene sediments were deposited unconformably over the Paleozoic basement and, in turn, are unconformably overlain by Pleistocene terrace and alluvial deposits. According to Muñiz et al. [22], the lower section can be correlated to sequence B of Sierro et al. [13], while the upper section would be connected to sequence E (Bonares Sands Formation), thus indicating the existence of a significant stratigraphic hiatus including at least part of the depositional sequences C and D, as suggested by Rodríguez-Tovar et al. [23].

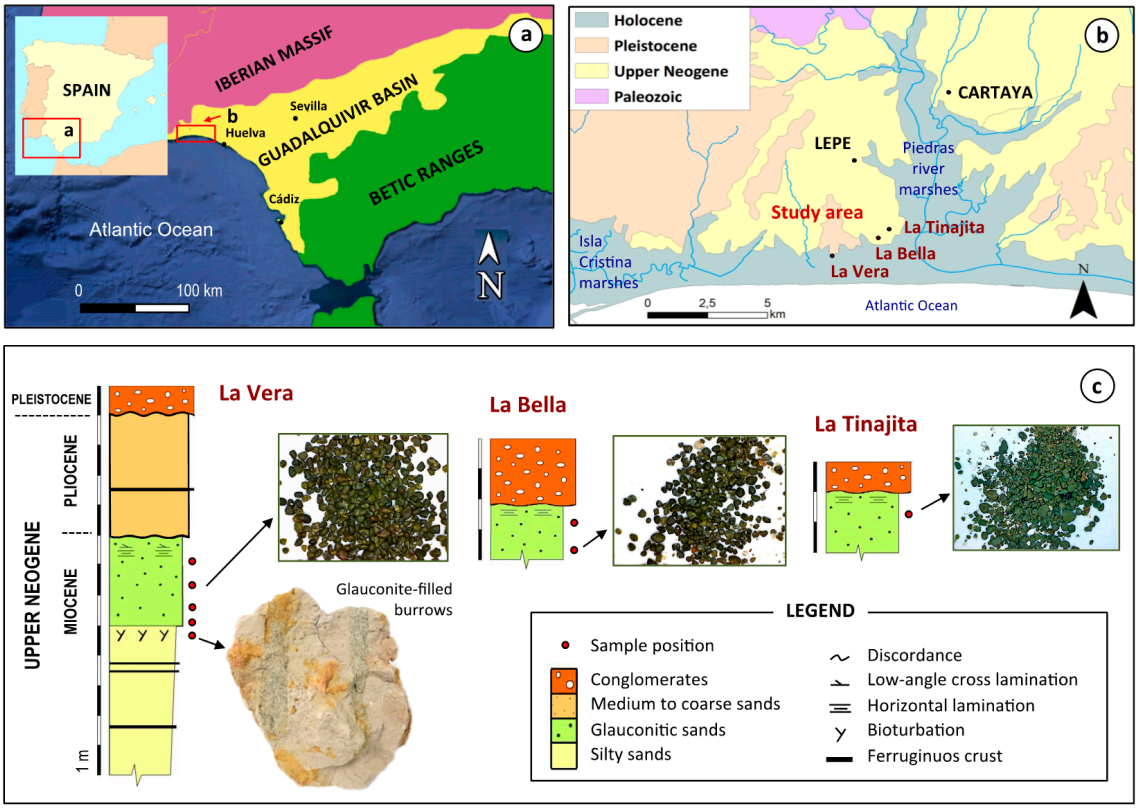

Figure 1. Generalized geological maps of the study area on a regional (**a**) and local (**b**) scale (adapted from IGME [24]), and schematic cross-sections of the exposures sampled for this study (**c**), showing the stratigraphic location of the green glauconitic sands.

3. Material and Methods

Eight representative samples of glauconite-bearing sediments were collected in three disconnected outcrops, namely, La Vera, La Bella and La Tinajita, of the lower glauconitic level (Figure 1c). The samples were sieved through 63 µm and 2 mm meshes to obtain the clean sand-size fraction. The clay fraction associated with the glauconitic condensed level was separated by centrifugation. Owing to its high paramagnetic susceptibility, the glauconite grains were magnetically separated from the non-magnetic sand fraction to a nearly pure glauconite concentrate, using a Frantz isodynamic separator with a current of 0.45 A, a longitudinal dip of 15°, and a transverse tilt of 20°. The concentrates were washed in deionized water, oven-dried at 60 °C, and then weighed to determine the percentage of glauconite by weight in each sample.

Firstly, some handpicked grains of the glauconite concentrates were examined under a binocular microscope to observe color and shapes. High-resolution back-scattered electron

(BSE) images were acquired using an environmental scanning electron microscope (ESEM) FEI Quanta 200 (FEI Co., Hillsboro, OR, USA), equipped with energy-dispersive X-ray detectors (EDS), in order to elucidate details of morphology, size and fabric. ImageJ software, a public domain Java image processing program, was used to measure basic shape parameters such as area, circularity (4πArea/perimeter^2), roundness (4Area/π major axis^2), and elongation of the granules.

The glauconite separate samples were gently ground into a fine powder using an agate mortar and pestle, and mineralogically characterized by X-ray diffraction (XRD) with a Bruker AXS D8-Advance diffractometer (Bruker Corp., Karlsruhe, Germany), using Cu-Kα radiation at 40 kV and 30 mA. Randomly oriented powders were scanned from 3 to 65° 2θ, with a step size of 0.02° and a counting time of 0.6 s per step. Oriented mounts of glauconite and clay separates were prepared and analyzed in the air-dried state, after solvation with ethylene glycol (60 °C for 48 h) and after heating (550 °C for 2 h). The oriented specimens were scanned from 1 to 30° 2θ using a step size of 0.02° and a step time of 1.2 s. The Pseudo-Voigt function was used to improve the measurement of positions, intensity and full width at half-maximum of the diffraction peaks, as well as to deconvolute overlapping peaks.

The major element composition of glauconite was determined in selected points of the examined granules, by electron probe microanalysis (EPMA) with a JEOL JXA-8200 SuperProbe (JEOL, Tokyo, Japan). The specimens were embedded in epoxy resin and polished to ensure optimal conditions for quantitative wavelength-dispersive (WDS) analysis, operating at 15 kV accelerating voltage, 20 nA beam current, and beam diameter of up to 5 μm. A suite of well-characterized minerals and synthetic materials was used as the standard for the calibration, and a conventional ZAF correction procedure was applied to correct for atomic number (Z), absorption (A), and fluorescence (F) effects.

Furthermore, thermo-gravimetric analysis (TGA) and differential scanning calorimetric (DSC) analysis were conducted to study the thermochemical decomposition behavior of glauconite, using a Mettler Toledo TG/DSC1 (Mettler Toledo, Greifensee, Switzerland) instrument equipped with STARe software (version 16.00, Mettler Toledo, Greifensee, Switzerland). The glauconite separates (20 mg) were placed into an open alumina crucible and heated from room temperature to 900 °C, at a constant heating rate of 10 °C/min^{-1}. All measurements were carried out under an oxygen flow of 20 mL/min^{-1}.

4. Results

4.1. Abundance, Physical Appearance and Occurrence

Glauconite abundance ranged widely, depending on the sampling location and the stratigraphic position of the samples. The largest concentration (21%) was found at the base of the glauconitic sand deposits outcropping at La Vera, while the lowest contents were observed at the La Bella and La Tinajita occurrences, in which glauconite made up less than 5% of the whole sample.

Under the binocular microscope, the glauconite concentrates from La Vera and La Bella exposures showed a dark green to almost black color that reflects high maturity, while those from La Tinajita consisted of pale to light green grains, likely corresponding to a less mature state. Brown and yellow-brown grains stained by iron oxides were also seen in glauconite sand, occurring as burrow infillings.

Overall, glauconite occurred as medium sand-sized grains ranging in diameter from 260 to 350 μm. The samples collected in the glaucony-rich deposit of La Vera showed granules up to 700 μm in size, with high mean values of circularity (about 0.78) and roundness (0.77), while the concentrate from La Bella was characterized by smaller and more elongate grains of glauconite, with an aspect ratio of 1.75:1.

Under SEM examination, glauconite exhibits considerable variety in habits and morphology (ovoidal, spheroidal, lobate, mammillary, and irregular-shaped), depending on the nature of the parent material subjected to glauconitization, the evolution stage, and the

effects of post-depositional disturbances. Three types of common substrates for glauconite formation were recognized (Figure 2):

1. Fecal pellets. Glauconite usually appears as round, smooth-surfaced ovoidal or spheroidal pellets, often with a distinct rim. Some glauconitized pellets display radial cracks that taper inward, without evidence of breakage. The pelletal glauconite from La Tinajita, unlike the other sites, is characterized by a concentric zoning pattern and rough surfaces with alteration halos along fractures.
2. Biogenic clasts. Glauconite occurs as fossil casts and internal molds that retain the shape of the original skeletal material by pseudomorphic replacement. Benthic foraminifera, with both spiral and serial arrangement of chambers, are the dominant biogenic substrate, followed occasionally by planktonic foraminifera and other biogenic clasts that resemble echinoderm ossicles and bryozoan fragments. The microfossil cavities appear to be filled with fine-grained flakes of glauconite.
3. Abiogenic clasts. Glauconite replaces detrital minerals, rock fragments and other non-biogenic clasts whose exact nature is difficult to determine, because their original shape was obliterated by glauconitization. Although glauconitic granules derived from slightly evolved fecal pellets may present inclusions of quartz and feldspars, these substrates were attributed to abiogenic clasts based on their high chemical maturity.

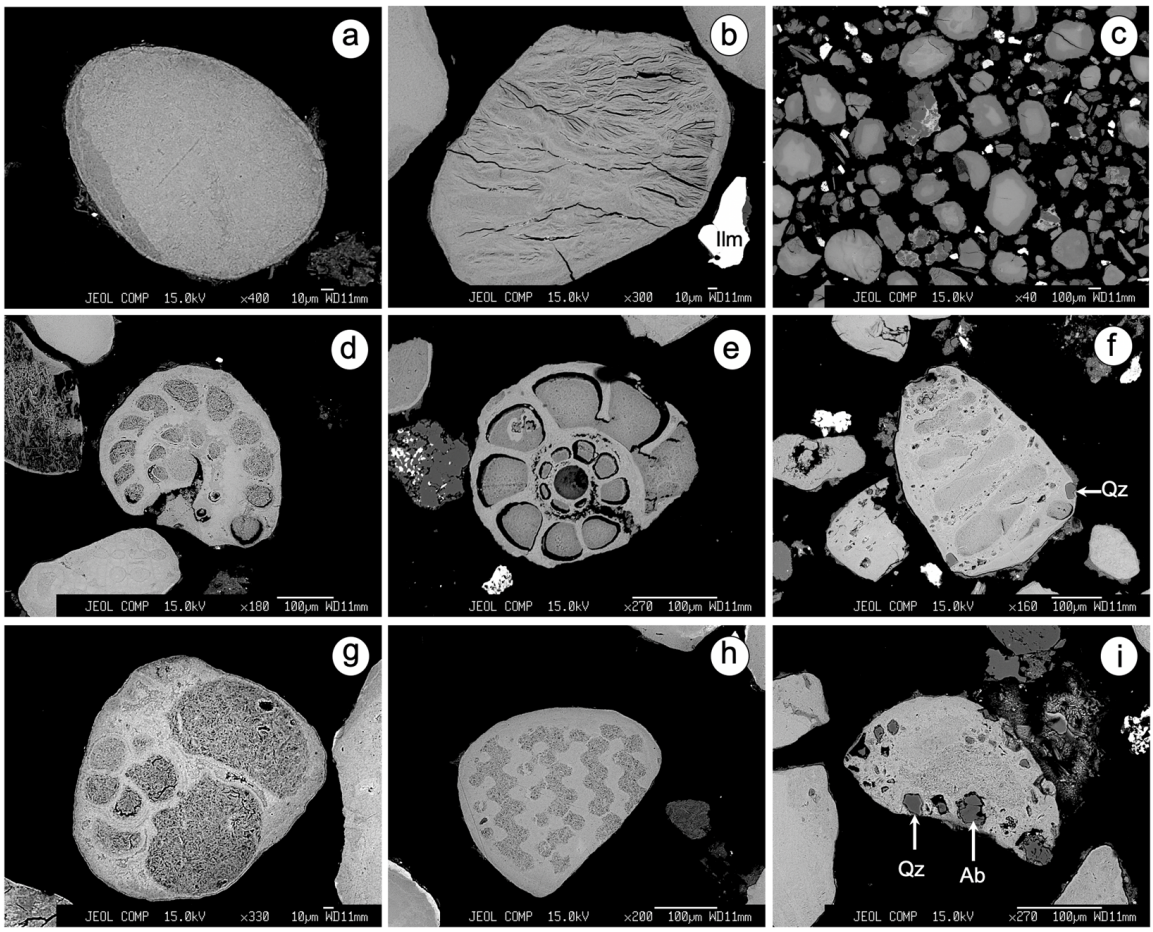

Figure 2. SEM/BSE images showing several types of glauconitized substrates: (**a**) well-rounded and ovoidal pellet; (**b**) pellet with internal radial cracks; (**c**) zoned grains from La Tinajita; (**d**) benthic foraminifera (order Rotaliida) with spiral chamber arrangement; (**d**) idem (order Ammonia); (**f**) biserial agglutinated benthic foraminifera (order Textulariida); (**g**) planktonic foraminifera; (**h**) fragment of echinoderm with a reticulate structure; (**i**) non-biogenic clast with tiny relicts of quartz and albite. Mineral abbreviations: Ab (albite); Ilm (ilmenite); Qz (quartz).

4.2. Mineralogy

The glauconite-bearing sediments systematically contain quartz and clay minerals with discrete amounts of alkaline feldspars. SEM-BSE imaging and EDS microanalysis revealed the presence of accessory minerals, such as ilmenite, hematite, rutile, aggregates of tabular crystals of jarosite pseudomorphs after pyrite, and fragments of ferruginous sandstones. The clay separates generally consisted of illite and kaolinite. In addition, smectite with marked swelling behavior upon ethylene glycolation was found in the clay fraction of the glauconitic horizon of La Vera (Figure 3a). Glauconitic mica was not detected in the <2 μm separates because it typically occurs in the sand fraction. A weak (002) reflection at ~5 Å is attributed to illite.

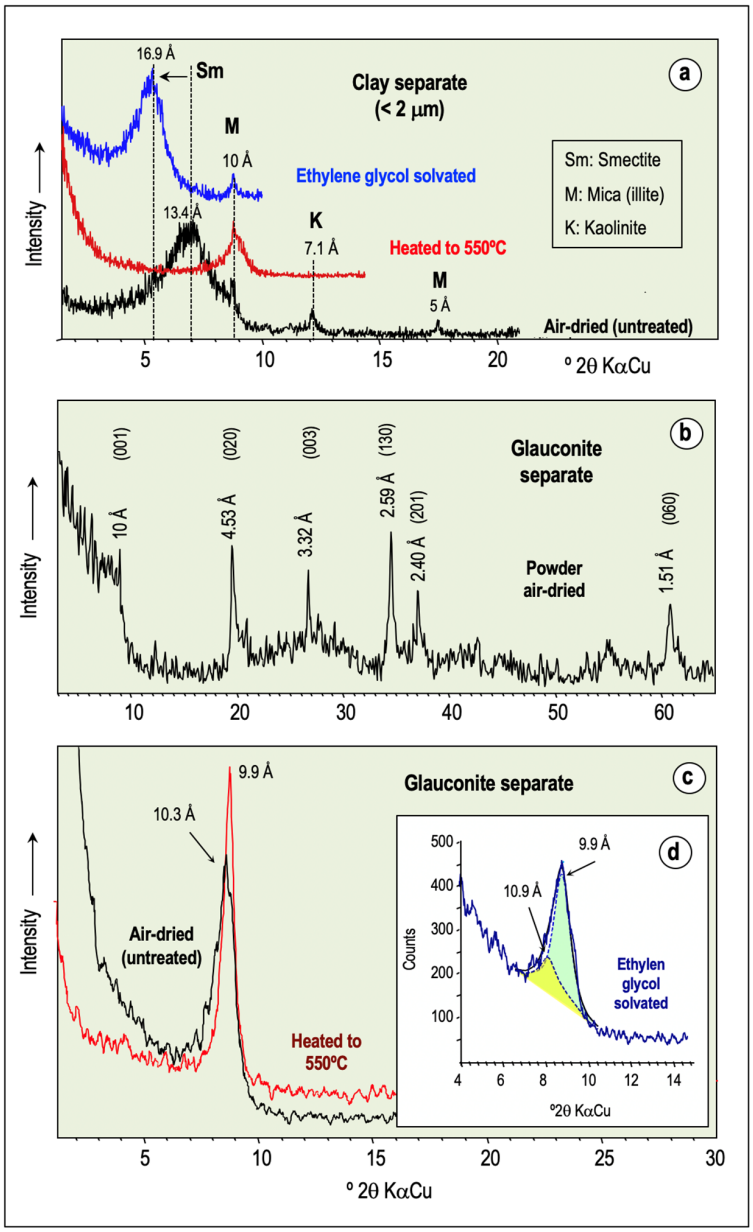

Figure 3. Representative XRD patterns of glaucony. Oriented aggregate diffractograms of clay separate in the air-dried state, and after heating to 500 °C and ethylene-glycol solvation (**a**); random powder diffractogram of glauconite separate (**b**); XRD diffractograms from oriented mounts of glauconite separate untreated and after heat-treatment (**c**); and deconvoluted (001) peak at ~10 Å after ethylene-glycol solvation treatment (**d**).

Powder XRD air-dried diagrams of the glauconite concentrates (Figure 3b) exhibit a series of sharp and narrow diffraction peaks at ~10 Å, 4.53 Å, 3.32 Å, 2.59 Å, 2.40 Å, and 1.51 Å spacings, among others, that can be assigned, respectively, to the reflections (001), (020), (003), (130), (201), and (060) of well-ordered glauconite. The first-order basal reflection (d_{001} ~10Å) does not exhibit a symmetrical sharp profile, but rather, a broad band that extends towards higher basal spacings, giving an average intensity maximum of 10.3 Å. This peak shifted to 9.9 Å on heating at 500 °C, and became more intense and fairly symmetrical upon heating (Figure 3c). After peak deconvolution of the samples solvated with ethylene glycol, the first basal reflection appears as an asymmetrical and wide band formed by two overlapping peaks at 9.9 Å and 10.9 Å spacings (Figure 3d), indicating that glauconite may contain some expandable smectite layers. According to López-Quirós et al. [2], the XRD patterns can be interpreted as a glauconite–smectite (R3 ordered) mixed-layer mineral comprised mainly of mica-type layers (>90%), based on the weak response to ethylene glycol solvation.

Thermogravimetric analysis of glauconite separates (Figure 4) showed a thermogravimetric curve (TG) and differential thermogravimetric curve (DTG) indicative of a first weight loss of 4–5%, associated with a low-temperature (80–200 °C) endothermic effect due to the removal of the interlayer and adsorbed water. A second weight loss of about 2–4% was observed in the range of 500–600 °C, corresponding to the dehydroxylation reaction of a glauconite with some expandable mixed layers [25] that are responsible for the loss of weight at low temperatures through dehydration.

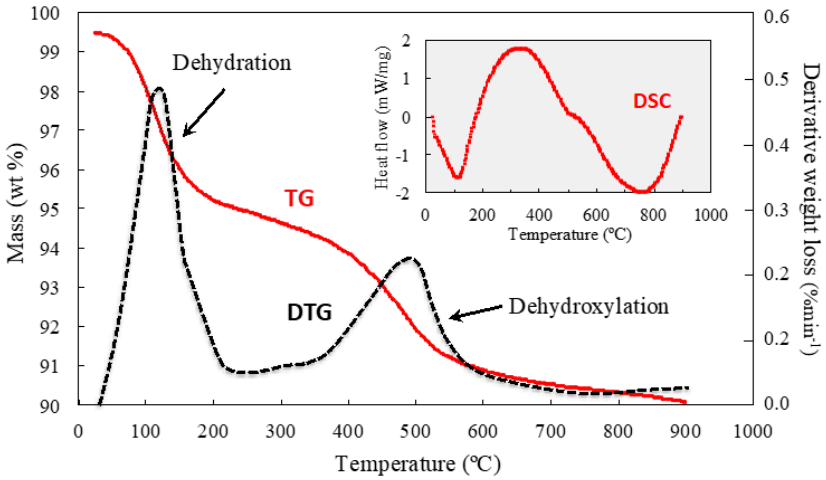

Figure 4. TG and DSC (inset) curves of glauconite concentrate. The derivative thermogravimetric (DTG) curve is also displayed, revealing two mass loss steps during the heating process.

4.3. Mineral Chemistry

The major element oxide composition of glauconite, determined on 63 points, varied from one grain to another and even within the same grain, depending on the nature of the substrate (Table 1). This grain-scale compositional heterogeneity is particularly apparent in the well-preserved foraminiferal tests from La Vera. The authigenic glauconite, occurring as infillings of foraminiferal chambers, has a higher content of Al_2O_3 and lower contents of Fe_2O_3 (total Fe recalculated as Fe_2O_3), K_2O and MgO than those of the glauconite that forms the test walls and septa. The pelletal glauconite is comparatively richer in Fe_2O_3 and K_2O relative to that occurring as the replacing material of foraminiferal tests.

The mean concentrations of TiO_2, MnO, CaO, Na_2O, and P_2O_5 are negligible and do not show any clear tendency. The pale green grains from La Tinajita clearly differ chemically from the others. They have a low silica content and display pronounced compositional zoning, defined by a rim-to-core increase in Fe_2O_3(t).

The Al_2O_3 content displays a significant ($p < 0.05$) negative correlation with Fe_2O_3(t), irrespective of the glauconitic substrate and stratigraphic position of the samples (Figure 5a).

A high negative correlation (R^2 = 0.74) was also found between Al_2O_3 and K_2O (Figure 5b), and K_2O appears to be positively interrelated with Fe_2O_3(t) (Figure 5c), as well as with MgO (Figure 5d), although there are some scattering of data points except perhaps at a low K content. No other significant correlations were observed among major elements.

Table 1. Averaged data from quantitative single-point EPMA microanalysis of glauconite grains (n = number of data points acquired). Each value represents the mean plus/minus one standard deviation. Total Fe expressed as Fe_2O_3.

Sampling Site	**La Vera**					**La Bella**	**La Tinajita**	
Substrate	**Foraminifera**		**Fecal Pellets**	**Burrow Infillings**	**Abiogenic Clasts**	**Fecal Pellets**	**Zoned Grains**	
Oxide (wt %)	**Walls n = 13**	**Chambers n = 9**	**n = 10**	**n = 12**	**n = 2**	**n = 11**	**Core n = 3**	**Rim n = 3**
SiO_2	47.61 ± 1.85	48.69 ± 1.50	48.19 ± 0.63	46.84 ± 1.40	48.27 ± 0.95	46.86 ± 0.89	33.50 ± 3.48	30.23 ± 3.51
Al_2O_3	6.06 ± 1.07	8.85 ± 2.16	4.51 ± 0.71	4.66 ± 0.92	6.72 ± 0.86	5.46 ± 1.09	5.57 ± 1.23	5.77 ± 1.07
TiO_2	0.04 ± 0.04	0.09 ± 0.05	0.04 ± 0.02	0.04 ± 0.04	0.07 ± 0.08	0.03 ± 0.04	0.39 ± 0.16	0.36 ± 0.12
Fe_2O_3(t)	29.11 ± 1.81	26.54 ± 1.44	29.88 ± 0.47	29.95 ± 2.05	27.26 ± 1.36	29.46 ± 0.92	37.62 ± 1.11	29.84 ± 2.58
MnO	0.03 ± 0.03	0.03 ± 0.02	0.02 ± 0.03	0.02 ± 0.02	0.02 ± 0.01	0.03 ± 0.02	0.01 ± 0.01	0.02 ± 0.02
MgO	4.11 ± 0.44	3.79 ± 0.56	4.29 ± 0.27	4.04 ± 0.37	4.29 ± 0.18	4.21 ± 0.18	3.17 ± 0.33	2.83 ± 0.28
CaO	0.20 ± 0.05	0.30 ± 0.12	0.18 ± 0.06	0.22 ± 0.09	0.28 ± 0.03	0.12 ± 0.05	0.05 ± 0.01	0.02 ± 0.01
Na_2O	0.04 ± 0.03	0.07 ± 0.05	0.05 ± 0.04	0.08 ± 0.07	0.14 ± 0.17	0.03 ± 0.02	0.02 ± 0.02	0.04 ± 0.03
K_2O	7.20 ± 0.51	5.76 ± 1.08	7.88 ± 0.48	7.54 ± 0.53	7.66 ± 0.05	8.06 ± 0.42	5.65 ± 0.89	4.89 ± 0.76
P_2O_5	0.15 ± 0.04	0.09 ± 0.03	0.10 ± 0.03	0.13 ± 0.07	0.12 ± 0.01	0.15 ± 0.03	0.40 ± 0.12	0.28 ± 0.08
Total	94.56 ± 1.66	94.21 ± 1.64	95.13 ± 0.45	93.51 ± 1.01	94.83 ± 0.17	94.42 ± 0.53	86.39 ± 2.16	74.28 ± 2.51

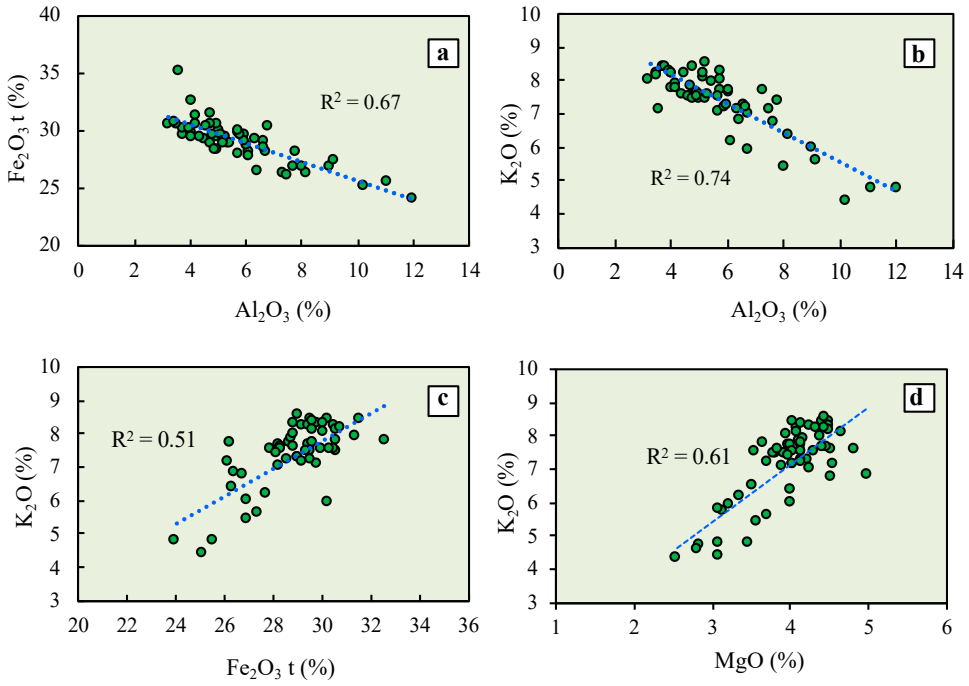

Figure 5. Bivariate plots showing the relationships between $Fe_2O_{3(t)}$ and Al_2O_3 (**a**); K_2O and Al_2O_3 (**b**); K_2O and $Fe_2O_{3(t)}$ (**c**); and K_2O and MgO (**d**). The dotted line is the linear regression fit.

The composition of individual glauconite grains was calculated on the basis of a half-unit cell with 10 oxygen atoms and 2 hydroxyls (22 negative charges) per formula unit, and assuming all measured Fe to be ferric. The average structural formulae (Table 2) show that the content of Si is nearly constant, with a value around 3.50 apfu in most grains, which implies the considerable replacement of Si by Al (0.42–0.49 apfu). In some glauconites, Fe^{3+} (up to 0.08 apfu) was needed to fill the tetrahedral sites. These cationic replacements lead to a negative tetrahedral charge of about 0.5 per half-unit cell.

Iron is the prevalent octahedral cation, ranging from 1.44 to 1.58 apfu, but subordinate amounts of Mg (0.41–0.47 apfu) and Al (up to 0.25 apfu) are also present in the octahedral sheet, which together account for a negative octahedral charge of between 0.11 and 0.32.

Thus, the isomorphic substitutions result in an overall net negative charge from 0.60 to 0.83. The resultant charge imbalance, arising mainly from Si-for-Al substitutions in the tetrahedral sheet, is compensated for by interlayer cations, mostly K^+. Calcium and Na^+ enter the interlayer space only as minor ions.

Table 2. Average structural formulae of glauconite calculated from EPMA results on the basis of 22 negative charges corresponding to $O_{10}(OH)_2$ per half-unit cell (n is the number of data points acquired).

Type of Substrate	Average Structural Formula
Foraminifera walls (n = 13)	$(K_{0.67}\ Na_{0.01}\ Ca_{0.02})_{0.70}\ (Fe^{3+}{}_{1.58}\ Al_{0.05}\ Mg_{0.45})_{2.08}\ (Si_{3.50}\ Al_{0.47}\ Fe^{3+}{}_{0.03})_4\ O_{10}\ (OH)_2$
Foraminifera chambers (n = 9)	$(K_{0.53}\ Na_{0.01}\ Ca_{0.02})_{0.56}\ (Fe^{3+}{}_{1.44}\ Al_{0.25}\ Mg_{0.41})_{2.10}\ (Si_{3.51}\ Al_{0.49})_4\ O_{10}\ (OH)_2$
Fecal pellets (n = 33)	$(K_{0.74}\ Na_{0.01}\ Ca_{0.01})_{0.76}\ (Fe^{3+}{}_{1.58}\ Al_{0.01}\ Mg_{0.46})_{2.05}\ (Si_{3.50}\ Al_{0.42}\ Fe^{3+}{}_{0.08})_4\ O_{10}\ (OH)_2$
Non-biogenic clasts (n = 2)	$(K_{0.71}\ Na_{0.02}\ Ca_{0.02})_{0.75}\ (Fe^{3+}{}_{1.50}\ Al_{0.09}\ Mg_{0.47})_{2.06}\ (Si_{3.51}\ Al_{0.49})_4\ O_{10}\ (OH)_2$

The mean content of interlayer K^+ ions ranges between 0.59 and 0.79 apfu, the mean ratio $^{VI}R^{2+}/(^{VI}R^{2+} + {}^{VI}R^{3+})$ is between 0.18 and 0.23, and the ratio $^{VI}Al/(^{VI}Al + {}^{VI}Fe^{3+})$ is close to zero, except for the chamber infills, in which the mean ratio is about 0.15 (Table 3). Such values fall within the typical range of the interlayer-deficient micas and are in good agreement with the composition of glauconite, defined by the International Mineralogical Association (IMA) and the Association Internationale pour l'Étude des Argiles (AIPEA) nomenclature committees [1].

Table 3. Averaged crystal–chemical data of glauconite obtained from the structural formulae. $^{VI}R^{2+}$ is represented by Mg cation and $(^{VI}R^{2+} + {}^{VI}R^{3+})$ by the sum of Mg, Fe and Al cations in the octahedral sheet. M is the number of interlayer cations and M^+ the interlayer charge; n is the number of data points acquired.

Sampling Site	Type	$^{VI}R^{2+}/(^{VI}R^{2+} + {}^{VI}R^{3+})$	$^{VI}Al/(^{VI}Al + {}^{VI}Fe)$	$\Sigma\ ^{XII}M$	$M^+(Si/4)^{-1}$	$^{VI}Fe/\Sigma^{VI}R$
La Vera	Foraminifera walls (n = 13)	0.22 ± 0.02	0.03 ± 0.03	0.70 ± 0.05	0.81 ± 0.06	0.76 ± 0.05
	Foraminifera chambers (n = 9)	0.19 ± 0.03	0.15 ± 0.09	0.56 ± 0.09	0.67 ± 0.10	0.68 ± 0.05
	Fecal pellets (n = 10)	0.23 ± 0.01	0	0.76 ± 0.04	0.87 ± 0.05	0.77 ± 0.01
	Burrow infillings (n = 12)	0.22 ± 0.02	0.01 ± 0.01	0.75 ± 0.04	0.88 ± 0.05	0.77 ± 0.01
	Abiogenic clasts (n = 2)	0.23 ± 0.01	0.06 ± 0.05	0.75 ± 0.03	0.88 ± 0.04	0.73 ± 0.04
La Bella	Fecal pellets (n = 11)	0.23 ± 0.01	0.01 ± 0.01	0.78 ± 0.04	0.91 ± 0.05	0.77 ± 0.01
La Tinajita	Core (n = 3)	0.18 ± 0.02	0	0.63 ± 0.09	0.88 ± 0.07	0.81 ± 0.01
	Rim (n = 3)	0.18 ± 0.01	0	0.62 ± 0.08	0.83 ± 0.05	0.81 ± 0.00

The crystal chemistry of the chamber infillings diverges from that of the walls and septa, indicating that compositional heterogeneity is effective not only from one grain to another but also within a grain, from one site to another. It is noteworthy that the layer charge of the glauconitic material preserved within the foraminiferal chambers was generally below 0.6. The cause for this layer charge deficit may be due to the occurrence of a smectite-rich smectite–glauconite interstratified mineral rather than, strictly speaking, a glauconite. This is in agreement with the XRD patterns, as the smectite layers are responsible for the change in position of the d_{001} peak observed after ethylene glycol treatment, and their K-deficient character.

When the compositional data are plotted in the cross-plot between the interlayer charge and the sum of octahedral cations (Figure 6), one can see that data points are widely scattered, and most of them fall outside the chemical composition domain of glauconite defined by Meunier and El Albani [26]. However, as noted previously, they fit the composition of glauconite proposed by IMA and AIPEA, which covers a broader compositional range. Many of our data points lie within the mica-rich glauconite-smectite interstratified mineral field of López-Quirós et al. [2], except those referring to the infillings of foraminiferal chambers, most of which fall within or near the Fe-montmorillonite compositional field. As it has a tetrahedral charge, and because its Fe content is much greater than its Al content, this smectite can be regarded as a phase, with a composition intermediate between nontronite and Fe-montmorillonite end-members [27].

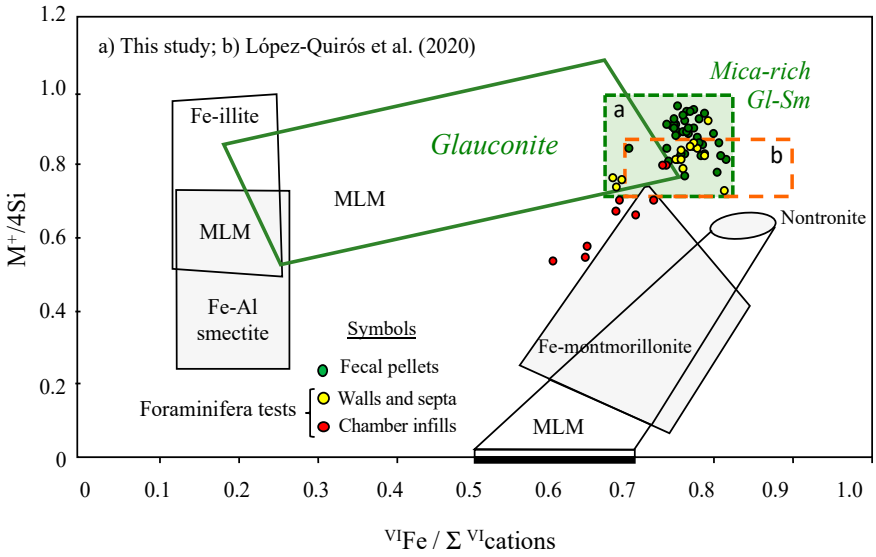

Figure 6. Projection of the chemical composition of glauconite pellets and foraminiferal tests in the $4M^+/Si$ vs. Fe/Σ^{VI} cation diagram of Meunier and El Albani [26], where M^+ is the total interlayer charge ($M^+ = Na + K + 2Ca$). The compositional domains of the Fe-bearing clay phases (Fe-illite, Fe-Al smectites and Fe-smectites) and the mica-rich glauconite-smectite mixed layers of López-Quirós et al. [2] are included for comparison. Mineral abbreviations: Gl (glauconite); Sm (smectite); MLM (mixed-layer minerals).

The percentage of glauconite in the mixed-layer clay mineral can be calculated using a logarithmic function model [2,28] that relates the percentage of mica-type layers with the interlayer K^+ ion content determined from the EPMA results (Figure 7). Thus, the pelletal glauconite can be ascribed to a glauconite-smectite mixed layer composed almost entirely of mica-type layers (97% on average), while the interlayer K^+ content is compatible with a glauconite-smectite mixed layer having around 93% of mica layers in the foraminiferal walls, and around 84% in the glauconite infillings within the chambers of foraminifera. Therefore, they are not the extreme form of glauconitic mica with 100% of mica layers, as interstratification with expandable smectite layers is always present in varying degrees.

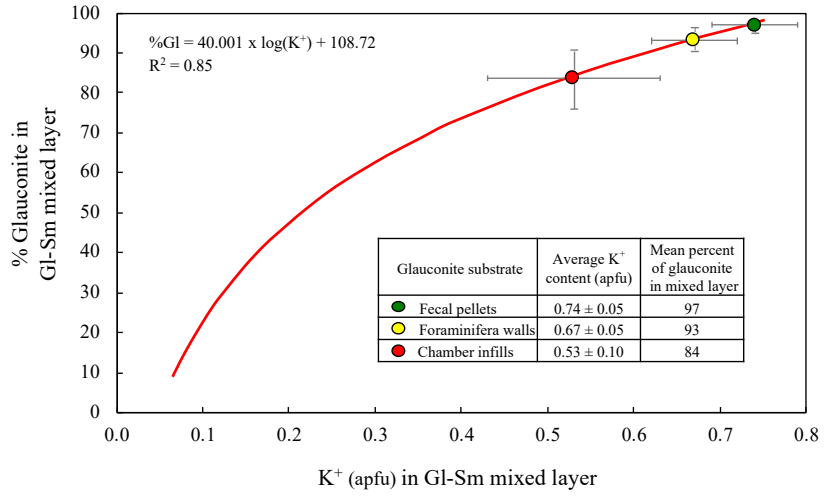

Figure 7. Percentage of glauconite layers in the glauconite-smectite mixed layer of the pellets and foraminiferal tests, estimated from the mean content of interlayer K^+ ions using the exponential trendline equation proposed by López-Quirós et al. [2] after Baldermann et al. [28]. Mineral abbreviations: Gl (glauconite); Sm (smectite).

5. Discussion

The green clay minerals of this study are interpreted to have been formed in situ and have not undergone significant reworking, although they show some evidence of post-depositional alteration. The first indication of the autochthonous origin of glaucony is the relatively low thickness (less than 3 m) of the glauconite-bearing condensed interval, and the close association of the glauconitic pellets with trace fossils and intensely burrowed sediments [29,30]. Another reliable indication of authigenesis is the scarcity of small fragments of broken pellets and the presence of deeply penetrating cracks within the glauconitic granules, which in turn is indicative of little or no appreciable transport [31,32]. These fractures likely formed due to the expansional growth of glauconite, which induces cracking at the grain surface. The glauconitic fillings observed inside well-preserved bioclasts can be regarded as authigenic clay minerals, because they also show no evidence of breakage.

Fecal pellets and benthic foraminiferal tests were the dominant substrates for glauconite authigenesis. Fecal pellets are relatively porous and usually contain a mixture of reactive organic matter and terrigenous clay minerals, and the calcareous shells of foraminifera are susceptible to dissolution, whereby both substrates were prone to glauconitization. They provide initially organic-rich, semi-confined microenvironments close to the sediment–seawater interface, with suitable post-depositional conditions for glauconite formation, as reported in previous studies [6,12,26].

It is generally thought that the concentrations of Fe^{3+} and K^+ in the seawater solution are too low to promote glauconite authigenesis by direct precipitation, but the glauconitic granules can gradually evolve from a neoformed Fe-rich smectite [33] through increased layer charge and K^+ fixation, to establish charge balance. In fact, the chemical composition of the glauconitic minerals reported here scatters in a relatively large domain of the $4M^+Si$ vs. $^{VI}Fe/\Sigma^{VI}$ cations cross-plot (Figure 8), extending from the field of highly evolved Fe-rich glauconites toward the Fe-smectite composition. Using the approach of Baldermann et al. [34], it can be inferred that the first stage of the glauconitization process is consistent with slow precipitation of an initial Fe-rich smectite-like phase in the pores of the fecal pellets and bioclast cavities, during a lengthy period of low sedimentation rate. The earliest phase to be formed was most likely an intergrade between nontronite and Fe-montmorillonite end-members, which evolved to an interstratified phase becoming, over time, more of a mica-rich glauconite–smectite mixed layer.

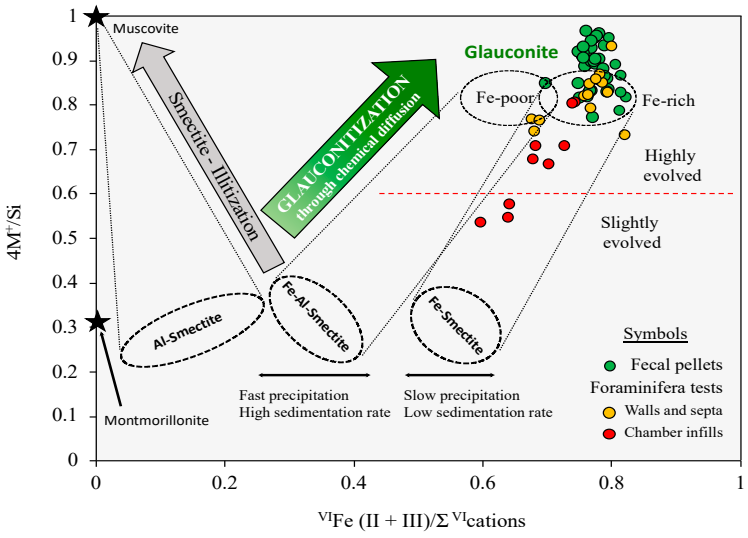

Figure 8. Projection of the glauconite pellets and foraminiferal tests in the $4M^+/Si$ vs. $^{VI}Fe(II + III)/\Sigma^{VI}$cations cross-plot of Baldermann et al. [34], depicting the path of the glauconitization process from a Fe-rich smectite precursor. The black stars represent the compositions of muscovite and montmorillonite.

5.1. Source and Geoavailability of Iron

A promoting factor for the initial precipitation of Fe-rich smectite was the abundance and geoavailability of iron. The radiometric age of glaucony in the study area (6.7 ± 0.3 Ma, according to Galán et al. [19]) is consistent with the timeframe (7–8 Ma) of the weathering processes that controlled the supergene alteration of the outcropping sulfide masses in the nearby continent (Iberian Pyrite Belt) during the Miocene [35], when uplifted and exposed at the surface, leading to the formation of gossans. During the Tortonian sedimentation, the foreland basin was in fact filled with clastic debris derived from the Paleozoic bedrock, including sulfide weathering products and gossanized rocks, due to terrigenous inputs from the surrounding continental margin to the sea.

Acid rock drainage waters likely played an important role in delivering Fe from the hinterland to the shelf sediments, as either nanoparticulate or dissolved materials, thereby contributing to the supply of iron needed for glauconite formation. Detrital amorphous Fe-oxides have been reported as the most effective Fe supplier in marine realms where glauconitic clays formed recently [36]. The large flux of continental sulfide weathering products probably resulted also in slightly acidic conditions that favored the development of glauconite from a Fe-rich smectite precursor [37].

The hinterland-derived weathering products were deposited on the oxic seafloor of the adjacent continental shelf. Under these oxidizing conditions, most of the Fe present in detrital sediments was in the trivalent oxidation state, primarily bound to Fe oxides and oxy-hydroxides like hematite and goethite. In this form, Fe was not originally available for uptake during glauconitization, thus preventing or limiting the authigenic formation of Fe-rich smectite and its subsequent transformation to glauconite. However, green-clay authigenesis was made possible by the prolonged residence time of the sediments at or near the interface between the oxidizing and reducing environments, where Fe^{3+} is transiently available as Fe^{2+} in solution [12,38].

Results from a study of the glaucony facies along the northern margin of the Guadalquivir Basin [39] provide evidence of the suboxic depositional setting, supported by a strong positive Ce-anomaly in glauconite and by the occurrence of pyrite and phosphorite nodules. Although pyrite was not observed in the sediments of the study area, the association of glauconitized pellets with jarosite, a secondary sulfate derived from sulfide oxidation under surface conditions, is an indirect indication of its primary occurrence.

The clay mineral assemblage of the marine mud was a heterogeneous mixture of illite, kaolinite and smectite, as inferred from XRD data. This clay fraction of the sediment matrix was probably the precursor material that filled the foraminiferal chambers after the death and decay of the organisms. Accumulation of terrigenous clayey material and Fe oxy-hydroxides nanoparticles inside foraminiferal chambers and other microfossil cavities might have occurred as a result of the gentle winnowing action of the bottom currents [40].

5.2. Glauconite-Forming Process

The results from this study are consistent with the most widely accepted conceptual reaction model proposed for glauconite authigenesis [2,6,28], which can be described as a two-step evolutionary process involving: (1) early diagenetic precipitation of a precursor Fe-smectite phase, and (2) the formation of mica-rich glauconite–smectite mixed layer through chemical maturation.

Our findings support the hypothesis that the redox conditions necessary to produce the solubilization of Fe(III) bound chemically to detrital minerals were achieved, at least locally, within fecal pellets, foraminiferal tests and their enclosing sediments, in which biogenic debris and bacterial activity imposed reducing conditions [26]. The microbial oxidation of organic matter would have enhanced the dissolution of Fe oxy-hydroxides, detrital clay minerals and carbonates under local, mildly reducing and slightly acidic conditions, as previously reported in the literature [28,30]. This implies that Fe and a variety of other elements, notably Si, Al, Mg and Ca, were released by reductive dissolution reactions into the surrounding seawater and pore fluids, thus providing a basic reservoir

of free ions in solution for the early diagenetic precipitation of Fe-smectite into the pores and cavities of the substrates. This precursor might have derived from a reaction between a Si-Al gel-like phase and Fe oxides [41].

Once mobilized by the reducing interstitial fluid, Fe^{2+} might have migrated inside the host substrates, where it was partly oxidized to Fe^{3+}, probably induced by the mineralization of organic matter and cessation of bacterial activity [26,42], and then stabilized in the octahedral sheets of the newly formed Fe-smectite. It can be assumed, therefore, that fecal pellets and microfossil cavities served as reducing microenvironments that counteracted the oxidizing seafloor conditions to produce, at the scale of the microsystem, the redox state initially required for starting the glauconitization.

During the progressive stages of early marine diagenesis, the Fe-smectite precursor phase is thermodynamically unstable [42] and was subsequently transformed into glauconite through the formation of glauconite–smectite mixed-layer minerals. The Fe-smectite to glauconite transformation can be viewed as a diffusion-controlled reaction [26] involving the slow diffusive transport of dissolved ions between the interstitial solution and the neoformed green clay.

Major chemical exchanges can be inferred from the statistical relationships between octahedral (Fe, Al and Mg) and interlayer (K) cations of the slightly evolved glauconitic fillings observed within the chambers of foraminiferal tests (Figure 9).

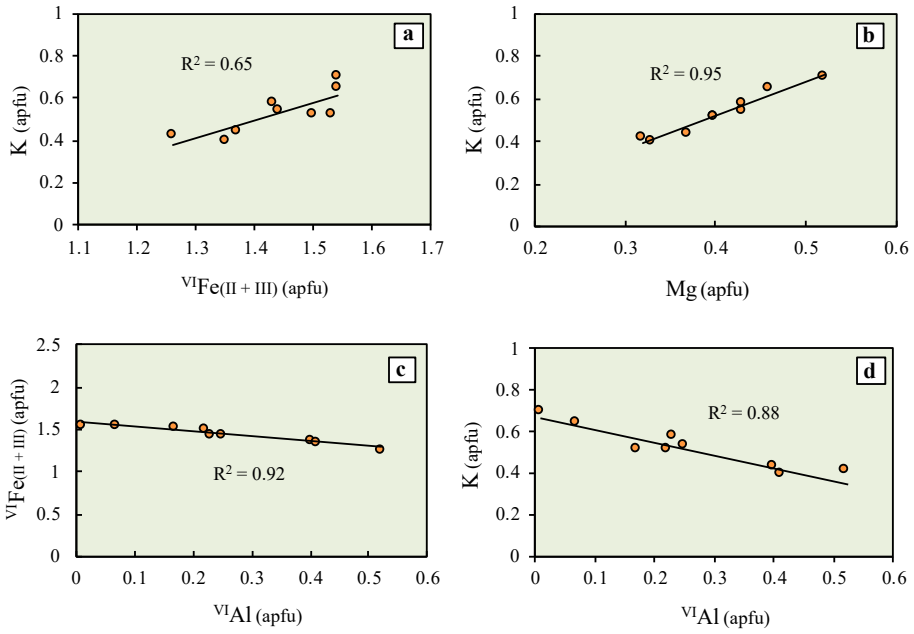

Figure 9. Bivariate plots displaying the relationships between major elements of the green clay within the chambers of foraminiferal tests: (**a**) K vs. ^{VI}Fe(II + III); (**b**) K vs. Mg; (**c**) ^{VI}Fe(II + III) vs. ^{VI}Al; and (**d**) K vs. ^{VI}Al. All values are expressed in atoms per formula unit (apfu). The solid line is the linear regression fit.

5.3. Chemical Maturity

The average K_2O content is generally used as the key indicator for assessing the chemical maturity or evolutionary state of glauconitization, because the concentration and activity of seawater K^+ ions have a strong influence on the progress of the glauconite-forming process [6,43]. Accordingly, most glauconitic pellets reached a moderate to high level of maturity, with mean K_2O values of 7.88% (La Vera) and 8.06% (La Bella), while the maturation state of the foraminiferal tests differed considerably depending on the domain studied: the walls and septa have a moderate maturity level (7.20% K_2O on average) and the chamber fillings are slightly evolved (5.76% K_2O on average). The dominant occurrence of pelletal glauconite in the high mature state indicates that glauconitization could have

taken between 10^5 and 10^6 years [10], which reflects a long period of residence at the sea water–sediment interface, in sediment-starved conditions, before burial.

As noted previously, it is clear that the interlayer incorporation of K^+ ions increased in the course of glauconitization and, therefore, the content of expandable smectite layers gradually decreased in the mixed-layer mineral, even though the degree of chemical maturity varied with the substrate nature. The high percentage of mica layers present in the pelletal glauconite suggests that the glauconitization process reacted almost to completion, due to the constant diffusion of seawater K^+ ions toward the substrate, and the sufficient supply of Fe available for uptake. In this type of substrate, the diffusion process was active until reaching highly mature grains, and most of the precursor Fe-smectite phase was transformed into a mica-rich glauconite–smectite interstratified with a mean composition of 97% mica layers and 3% smectite layers.

The foraminiferal tests are in different stages of evolution, even within a single grain. The glauconite-smectite mixed layers of the walls and septa are composed of 93% mica layers and 7% smectite layers on average, whereas the chamber infillings are mixed-layer minerals consisting of 84% mica layers and 16% smectite layers. A plausible explanation for this decreased maturity in the green clay fillings is that the glauconitization process was stopped at an early stage before completion of the reaction, probably due to a disruption of the ion diffusion regime. The formation of dense, impermeable microstructures during glauconite maturation [44] caused a dramatic loss of microporosity and permeability in the shell material through cementation, thereby reducing the rate of diffusion between the foraminiferal chambers and the interstitial solution. The supply of K^+ ions might also have been hindered by fine sediments clogging the tiny pores (5 μm) of foraminifera [45]. In any case, the result is that the loss of microporosity limited the maturation process of glauconite within the foraminiferal tests.

As a general summary, an overall sketch illustrating the evolutionary process of glauconitization proposed in this study, for both fecal pellets and foraminiferal tests, is shown in Figure 10.

5.4. Post-Depositional Weathering

Glauconitic minerals are highly stable and resistant to dissolution in the marine environment [46]; however, they tend to destabilize in weathering profiles. In fact, glauconite grains showed some evidence of post-depositional alteration as a result of chemical weathering processes (Figure 11).

The pelletal glauconite from La Vera and La Bella often appears surrounded by a thick rim (<10 μm) (Figure 11a), chemically composed mainly of Fe (up to 64% $Fe_2O_{3(t)}$) and other immobile elements like Al (up to 10.2% Al_2O_3) and Ti (up to 2.14% TiO_2). The rims are usually made up of nanometric inclusions of iron oxy-hydroxides, according to High Resolution Transmission Electron Microscopy (HRTEM) observations made elsewhere [47], and probably contain some kaolinite, which are the common products of glauconite alteration under weathering conditions [48]. The ferruginous rims have encapsulated some of the glauconite granules and sealed their surface cracks, protecting them against advanced weathering and fragmentation.

Another indication of supergene alteration is the formation of jarosite at the expense of pyrite closely associated with glauconite, as detected by SEM-EDS in various granules (Figure 11b). It is noteworthy that the glauconite granules affected by this process showed a decrease of about 25% in the K_2O content with respect to the average value of the unweathered glauconite. The hydrogen ions (H^+) released by the oxidative dissolution of pyrite created an acidic microenvironment favorable to producing partial hydrolysis of nearby glauconite grains. As a result of this hydrolytic action, the K^+ ions were removed from the interlayer spaces of glauconite and became available in the aqueous solution, to combine with Fe^{3+} and sulfate ions released by pyrite (FeS_2) oxidation, thus forming jarosite ($KFe_3(SO_4)_2(OH)_6$) through the following reactions:

$$FeS_2 + 7/2O_2 + H_2O \rightarrow Fe^{2+} + 2{SO_4}^{2-} + 2H^+$$

$$2Fe^{2+} + 1/2O_2 + 2H^+ \rightarrow 2Fe^{3+} + H_2O$$

$$K^+ + 3Fe^{3+} + 2SO_4{}^{2-} + 7H_2O \rightarrow KFe_3(SO_4)_2(OH)_6 + 6H^+$$

The compositional zoning displayed by the vast majority of the pale green glauconitic pellets from the La Tinajita occurrence (Figure 11c) can be also attributed to post-depositional effects. The EPMA data revealed that there is a decrease in the $Fe_2O_{3(t)}$, K_2O and MgO contents of the glauconitic material toward the periphery of the grains, as well as along the fractures, and an increase in the Al_2O_3 content relative to the cores, thus following a pattern similar to the reverse glauconitization [5,49]. This concentric zoning is typical of glauconite that undergoes degradation by the action of meteoric water [50].

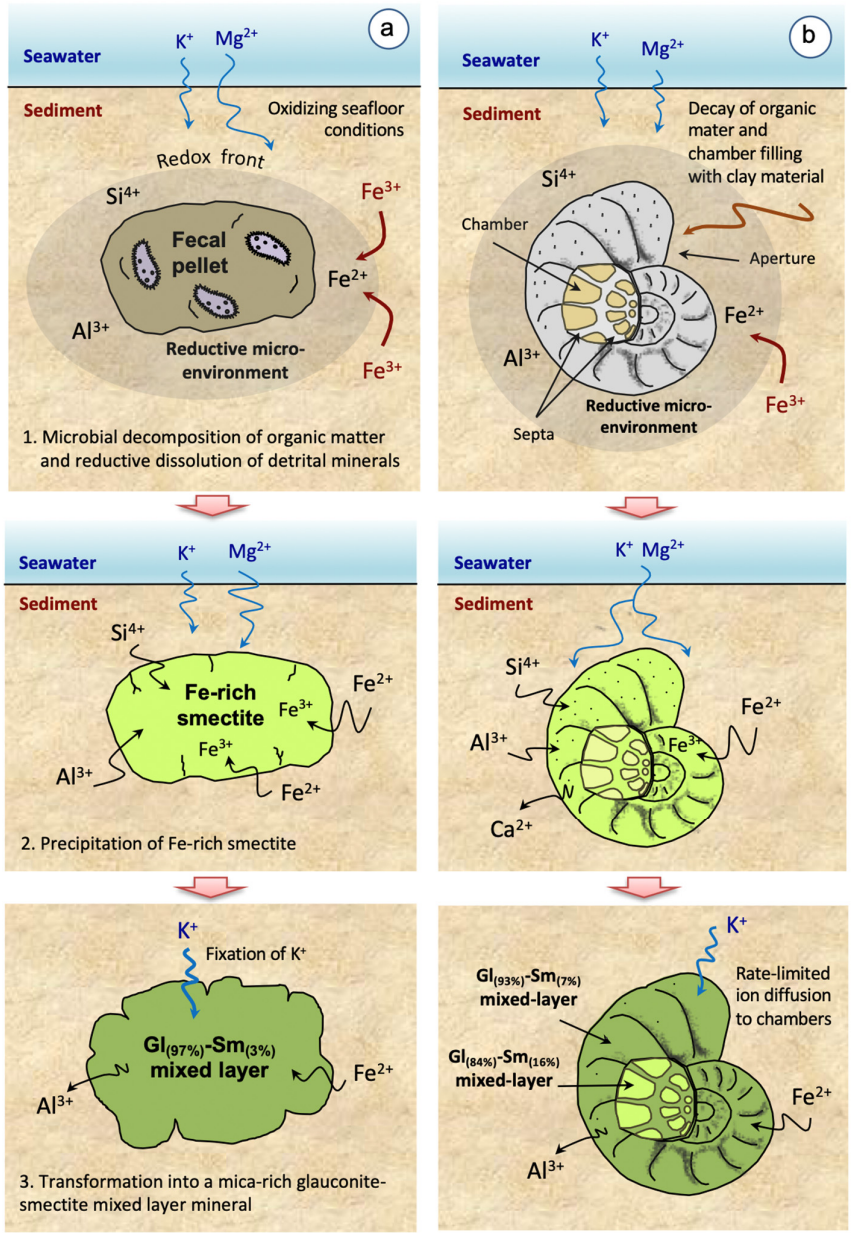

Figure 10. Schematic evolution of the glauconitization process in fecal pellets (**a**) and foraminiferal tests (**b**), highlighting the three main stages involved in the development of glauconitic minerals (see explanation in the text for details).

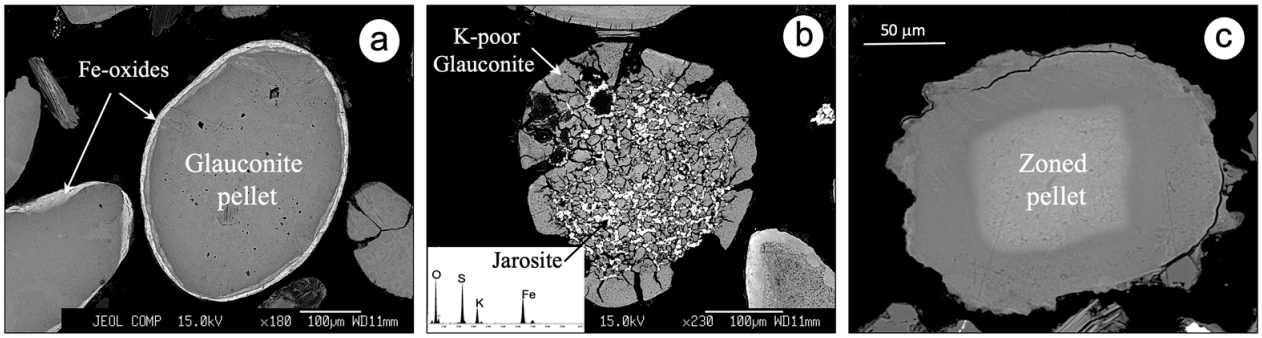

Figure 11. SEM/BSE images showing certain effects due to post-depositional evolution: an ovoidal glauconite pellet rimmed by Fe oxides (**a**); a K-poor glauconite associated with jarosite (**b**); a zoned pellet from La Tinajita in which the change from the inner to the outer zone is marked by a decrease in the contents of $Fe_2O_{3(t)}$ and K_2O (**c**). Scale bar (**c**): 50 µm.

6. Concluding Remarks

This study has revealed that green marine clay of the glaucony facies is heterogeneous in mineral and chemical composition, reflecting a complex interaction of substrate influences, environmental factors, and post-depositional effects. Highly porous substrates, a reductive microenvironment, sufficient iron availability, and residence for lengthy periods at or near the water–sediment boundary (depositional hiatus) have been suggested as some of the key factors driving the glauconite-forming process. A range of recognizable substrates was susceptible to glauconitization, with fecal pellets and foraminiferal tests being the most favorable. However, not all substrates were equally conducive to the progress of the reaction, as evidenced by the occurrence of glauconite at different evolutionary stages in the same stratigraphic level. The proportion of mica-type layers in the glauconite–smectite mixed layers seems to be a reasonable basis for distinguishing between the various evolutionary stages. The glauconite pellets reached the most evolved stage, with 97% of mica layers on average, while the bioclasts displayed different degrees of maturation, even within a single grain, ranging from 84% (chamber infillings) to 93% (shell replacements) of mica layers. The results highlight the importance of addressing this grain-scale compositional heterogeneity if the glauconitization process is to be accurately documented, and glauconite is to be used for the isotopic dating of condensed stratigraphic sections. For geochronological purposes, the highly evolved, K-rich pelletal glauconite grains should be exclusively selected.

Author Contributions: Conceptualization, J.C.F.-C.; formal analysis, S.F.-L.; investigation, S.F.-L.; methodology, J.C.F.-C., supervision, J.C.F.-C.; writing—original draft, S.F.-L.; writing—review & editing, J.C.F.-C. All authors have read and agreed to the published version of the manuscript.

Funding: This research received no external funding.

Data Availability Statement: The authors confirm that the data supporting the findings of this study are available within the manuscript. Raw data are available upon reasonable request.

Acknowledgments: We thank Fernando Muñiz (University of Seville) for its collaboration during fieldwork, Josep Tosquella (University of Huelva) for helping with microfossil identification, and Jesús Díaz (University of Huelva) for assistance with thermal analysis. The authors greatly appreciate the quick and valuable review of the manuscript by three anonymous referees.

Conflicts of Interest: The authors declare that they have no conflict of interest or competing financial interests.

References

1. Rieder, M.; Cavazzini, G.; Yakonov, Y.S.; Frank-Kamenetskii, V.A.; Gottardi, G.; Guggenheim, S.; Koval, P.V.; Müller, G.; Neiva, A.M.R.; Robert, J.L.; et al. Nomenclature of the micas. *Mineral. Mag.* **1999**, *63*, 267–279. [CrossRef]
2. López-Quirós, A.; Sánchez-Navas, A.; Nieto, F.; Escutia, C. New insights into the nature of glauconite. *Am. Mineral.* **2020**, *105*, 674–686. [CrossRef]

3. Odin, G.S.; Létolle, R. Glauconitization and phosphatization environments: A tentative comparison. In *Marine Phosphorites*; Bentor, Y.K., Ed.; SEPM Society for Sedimentary Geology, Spec. Publ.: McLean, VA, USA, 1980; Volume 29, pp. 227–237.
4. Amorosi, A. The occurrence of glaucony in the stratigraphic record: Distribution patterns and sequence-stratigraphic significance. In *Linking Diagenesis to Sequence Stratigraphy*, 1st ed.; Morad, S., Ketzer, J.M., De Ros, L.F., Eds.; International Association of Sedimentologists, Spec. Publ.: Gent, Belgium, 2013; Volume 45, pp. 37–53.
5. López-Quirós, A.; Escutia, C.; Sánchez-Navas, A.; Nieto, F.; García-Casco, A.; Martín-Algarra, A.; Evangelinos, D.; Salabarnada, A. Glaucony authigenesis, maturity and alteration in the Weddell Sea: An indicator of paleoenvironmental conditions before the onset of Antarctic glaciation. *Sci. Rep.* **2019**, *9*, 13580. [CrossRef] [PubMed]
6. Odin, G.S.; Matter, A. De Glauconiarum Origine. *Sedimentology* **1981**, *28*, 611–641. [CrossRef]
7. Banerjee, S.; Bansal, U.; Thorat, A.V. A review on palaeogeographic implications and temporal variation in glaucony composition. *J. Palaeogeogr.* **2016**, *5*, 43–71. [CrossRef]
8. Burst, J.F. "Glauconite" pellets: Their mineral nature and applications to stratigraphic interpretations. *Am. Assoc. Petrol. Geol. Bull.* **1958**, *42*, 310–327.
9. Hower, J. Some factors concerning the nature and the origin of glauconite. *Am. Mineral.* **1961**, *46*, 313–334.
10. Odin, G.S. *Green Marine Clays; Developments in Sedimentology*, 1st ed.; Elsevier: Amsterdam, The Netherlands, 1988; Volume 45, 444p.
11. Dasgupta, S.; Chaudhuri, A.K.; Fukuoka, M. Compositional characteristics of glauconitic alterations of K-feldspar from India and their implications. *J. Sediment. Petrol.* **1990**, *60*, 277–281.
12. Baldermann, A.; Grathoff, G.H.; Nickel, C. Micromilieu-controlled glauconitization in fecal pellets at Oker (Central Germany). *Clay Miner.* **2012**, *47*, 513–538. [CrossRef]
13. Sierro, F.J.; González-Delgado, J.A.; Dabrio, C.J.; Flores, J.A.; Civis, J. Late Neogene depositional sequences in the foreland basin of Guadalquivir (SW Spain). In *Tertiary Basins of Spain: The Stratigraphic Record of Crustal Kinematics*, 1st ed.; Friend, P.F., Dabrio, C.J., Eds.; Cambridge University Press: Cambridge, UK, 1996; Volume 6, pp. 339–345.
14. Civis, J.; Sierro, F.J.; González Delgado, J.A.; Flores, J.A.; Andrés, L.; de Porta, J.; Valle, M.E. El Neógeno marino de la provincia de Huelva: Antecedentes y definición de las unidades litoestratigráficas. In *Paleontología del Neógeno de Huelva (W. Cuenca del Guadalquivir)*, 1st ed.; Civis, J., Ed.; Universidad de Salamanca: Salamanca, Spain, 1987; pp. 9–21.
15. Mayoral, E.; Pendón, J.G. Icnofacies y sedimentación en zona costera. Plioceno superior (?), litoral de Huelva. *Acta Geol. Hispánica* **1986–1987**, *21–22*, 507–513.
16. Baceta, J.I.; Pendón, J.G. Estratigrafía y arquitectura de facies de la Formación Niebla, Neógeno superior, sector occidental de la Cuenca del Guadalquivir. *Rev. Soc. Geol. Esp.* **1999**, *12*, 419–438.
17. Galán, E.; González, I.; Mayoral, E.; Vázquez, M.A. Caracterización y origen de la facies glauconítica de la cuenca del Guadalquivir. *Estud. Geol.* **1989**, *45*, 169–175. [CrossRef]
18. Abad, M.; De La Rosa, J.; Pendón, J.G.; Ruiz, F.; González-Regalado, M.L.; Tosquella, J. Caracterización geoquímica del horizonte glauconítico en el límite superior de la Formación Niebla (Tortoniense superior, SO España): Datos preliminares. *Geogaceta* **2004**, *35*, 35–38.
19. Galán, E.; González, I.; Mayoral, E.; Muñiz, F. Contribution of clay mineralogy to the paleoenvironmental interpretation of upper Miocene detrital sediments. Southwestern Iberian Peninsula. In *Euroclay'95, Book of Abstracts*; Elsen, A., Grobet, P., Keung, M., Leeman, H., Schoonheydt, R., Toufar, H., Eds.; Louvain University: Louvain-la-Neuve, Belgium, 1995; pp. 311–312.
20. Gonzalez, R.; Dias, J.M.A.; Lobo, F.; Mendes, I. Sedimentological and paleoenvironmental characterisation of transgressive sediments on the Guadiana Shelf (Northern Gulf of Cádiz, SW Iberia). *Quat. Int.* **2004**, *120*, 133–144. [CrossRef]
21. Belaústegui, Z.; Muñiz, F.; Mángano, M.G.; Buatois, L.A.; Domènech, R.; Martinell, J. *Lepeichnus giberti* igen. nov. isp. nov. from the upper Miocene of Lepe (Huelva, SW Spain): Evidence for its origin and development with proposal of a new concept, ichnogeny. *Palaeogeogr. Palaeocl. Palaeoecol.* **2016**, *452*, 80–89. [CrossRef]
22. Muñiz, F.; Mayoral, E.; Cáceres, L.M.; Cachão, M. Correlación entre las unidades litoestratigráficas del Neógeno Superior en el sector occidental de la Península Ibérica. *Geogaceta* **2001**, *30*, 243–244.
23. Rodríguez-Tovar, F.J.; Dorador, J.; Mayoral, E.; Santos, A. Outcrop and core integrative ichnofabric analysis of Miocene sediments from Lepe, Huelva (SW Spain): Improving depositional and paleoenvironmental interpretations. *Sediment. Geol.* **2017**, *349*, 62–78. [CrossRef]
24. IGME. *Mapa Geológico de España a escala 1:50.000. Hojas nº 998 (Ayamonte) y 999 (Huelva)*; Instituto Geológico y Minero de España: Madrid, Spain, 1973/1979.
25. Földvari, M. *Handbook of Thermogravimetric System of Minerals and its Use in Geological Practice*; Geological Institute of Hungary: Budapest, Hungary, 2011; p. 180.
26. Meunier, A.; El Albani, A. The glauconite-Fe-illite-Fe-smectite problem: A critical review. *Terra Nova* **2007**, *19*, 95–104. [CrossRef]
27. Petit, S.; Caillaud, J.; Righi, D.; Madejová, J.; Elsass, F.; Köster, H.M. Characterization and crystal chemistry of an Fe-rich montmorillonite from Ölberg, Germany. *Clay Miner.* **2002**, *37*, 283–297. [CrossRef]
28. Baldermann, A.; Warr, L.N.; Grathoff, G.H.; Dietzel, M. The rate and mechanism of deep-sea glauconite formation at the Ivory Coast—Ghana marginal ridge. *Clays Clay Miner.* **2013**, *61*, 258–276. [CrossRef]
29. Amorosi, A. Detecting compositional, spatial, and temporal attributes of glaucony: A tool for provenance research. *Sediment. Geol.* **1997**, *109*, 135–153. [CrossRef]

30. El Albani, A.; Meunier, A.; Fürsich, F. Unusual occurrence of glauconite in a shallow lagoonal environment (Lower Cretaceous, northern Aquitaine Basin, SW France). *Terra Nova* **2005**, *17*, 537–544. [CrossRef]
31. Banerjee, S.; Bansal, U.; Pande, K.; Meena, S.S. Compositional variability of glauconites within the Upper Cretaceous Karai Shale Formation, Cauvery Basin, India: Implications for evaluation of stratigraphic condensation. *Sediment. Geol.* **2016**, *331*, 12–29. [CrossRef]
32. Choudhury, T.R.; Banerjee, S.; Khanolkar, S.; Saraswati, P.K.; Meena, S.S. Glauconite authigenesis during the onset of the Paleocene-Eocene Thermal Maximum: A case study from the Khuiala Formation in Jaisalmer Basin, India. *Palaeogeogr. Palaeocl. Palaeoecol.* **2021**, *571*, 110388. [CrossRef]
33. Sánchez-Navas, A.; Martín-Algarra, A.; Nieto, F. Bacterially-mediated authigenesis of clays in phosphate stromatolites. *Sedimentology* **1998**, *45*, 519–533. [CrossRef]
34. Baldermann, A.; Dietzel, M.; Mavromatis, V.; Mittermayr, F.; Warr, L.N.; Wemmer, K. The role of Fe on the formation and diagenesis of interstratified glauconite-smectite and illite-smectite: A case study of Upper Cretaceous shallow-water carbonates. *Chem. Geol.* **2017**, *453*, 21–34. [CrossRef]
35. Velasco, F.; Herrero, J.M.; Suárez, S.; Yusta, I.; Alvaro, A.; Tornos, F. Supergene features and evolution of gossans capping massive sulphide deposits in the Iberian Pyrite Belt. *Ore Geol. Rev.* **2013**, *53*, 181–203. [CrossRef]
36. Giresse, P.; Wiewióra, A. Stratigraphic condensed deposition and diagenetic evolution of green clay minerals in deep water sediments on the Ivory Coast-Ghana Ridge. *Mar. Geol.* **2001**, *179*, 51–70. [CrossRef]
37. Zhang, X.; Cai, Y.; Jiang, D.; Zhang, Y.; Pan, Y.; Bai, L. An experimental study on transforming montmorillonite to glauconite: Implications for the process of glauconitization. *Clays Clay Miner.* **2017**, *65*, 431–448. [CrossRef]
38. Ireland, B.J.; Curtis, C.D.; Whiteman, J.A. Compositional variation within some glauconites and illites and implications for their stability and origins. *Sedimentology* **1983**, *30*, 769–786. [CrossRef]
39. Abad, M. La Transgresión Tortoniense en el Margen Pasivo de la Cuenca del Guadalquivir: Respuesta Estratigráfica e Implicaciones Paleontológicas. Ph.D. Thesis, University of Huelva, Spain, 2007. Unpublished work.
40. Wiewióra, A.; Giresse, P.; Petit, S.; Wilamowksi, A. A deep-water glauconitization process on the Ivory Coast-Ghana marginal ridge (ODP Site 959): Determination of Fe^{3+}-rich montmorillonite in green grains. *Clays Clay Miner.* **2001**, *49*, 540–558. [CrossRef]
41. Jiménez-Millán, J.; Castro, J.M. K-feldspar alteration to gel material and crystallization of glauconitic peloids with berthierine in Cretaceous marine sediments—sedimentary implications (Prebetic Zone, Betic Cordillera, SE Spain). *Geol. J.* **2008**, *43*, 19–31. [CrossRef]
42. Gaudin, A.; Buatier, M.D.; Beaufort, D.; Petit, S.; Grauby, O.; Decarreau, A. Characterization and origin of Fe^{3+}-montmorillonite in deep-water calcareous sediments (Pacific Ocean, Costa Rica margin). *Clays Clay Miner.* **2005**, *53*, 452–465. [CrossRef]
43. Amorosi, A.; Sammartino, I.; Tateo, F. Evolution patterns of glaucony maturity: A mineralogical and geochemical approach. *Deep Sea Res. Part II Top. Stud. Oceanogr.* **2007**, *54*, 1364–1374. [CrossRef]
44. Stille, P.; Clauer, N. The process of glauconitization: Chemical and isotopic evidence. *Contrib. Mineral. Petrol.* **1994**, *117*, 253–262. [CrossRef]
45. Banerjee, S.; Chattoraj, S.L.; Saraswati, P.K.; Dasgupta, S.; Sarkar, U. Substrate control on formation and maturation of glauconites in the Middle Eocene Harudi Formation, western Kutch, India. *Mar. Petrol. Geol.* **2012**, *30*, 144–160. [CrossRef]
46. Harding, S.C.; Nash, B.P.; Petersen, E.U.; Ekdale, A.A.; Bradbury, C.D.; Dyar, M.D. Mineralogy and geochemistry of the Main Glauconite Bed in the Middle Eocene of Texas: Paleoenvironmental implications for the verdine facies. *PLoS ONE* **2014**, *9*, e87656. [CrossRef] [PubMed]
47. Sánchez-Navas, A.; Martín-Algarra, A.; Eder, V.; Jagannadha-Reddy, B.; Nieto, F.; Zanin, Y.N. Color, mineralogy and composition of Upper Jurassic West Siberian glauconite: Useful indicators of paleoenvironment. *Can. Mineral.* **2008**, *46*, 1249–1268. [CrossRef]
48. Velde, B. Green clay minerals. In *Treatise on Geochemistry*; MacKenzie, F.T., Ed.; Elsevier: Amsterdam, The Netherlands, 2003; Volume 7, pp. 309–324.
49. Velde, B. *Clay Minerals—A Physico-Chemical Explanation of their Occurrence; Developments in Sedimentology*, 1st ed.; Elsevier: Amsterdam, The Netherlands, 1985; Volume 40, 426p.
50. Bansal, U.; Banerjee, S.; Pande, K.; Arora, A.; Meena, S.S. The distinctive compositional evolution of glauconite in the Cretaceous Ukra Hill Member (Kutch basin, India) and its implications. *Mar. Petrol. Geol.* **2017**, *82*, 97–117. [CrossRef]